Magnetic and Mössbauer characterization of the multiferroic fluoride K₃Fe₅F₁₅

F. Mezzadri,[1,*] G. Calestani,[1,2] C. Pernechele,[3] M. Solzi,[3] G. Spina,[4] L. Cianchi,[5] F. Del Giallo,[5] M. Lantieri,[5] M. Buzzi,[3] and E. Gilioli[2]

[1]*Dipartimento di Chimica GIAF, Università di Parma, Area delle Scienze 17/A, 43124 Parma, Italy*
[2]*IMEM-CNR, Area delle Scienze 37/A, 43124 Parma, Italy*
[3]*Dipartimento di Fisica, Università di Parma, Area delle Scienze 7/A, 43124, Italy*
[4]*Dipartimento di Fisica, Università di Firenze, 50019 Sesto Fiorentino (FI), Italy*
[5]*Istituto dei Sistemi Complessi, CNR, 50019 Sesto Fiorentino (FI), Italy*
(Received 8 April 2011; revised manuscript received 20 July 2011; published 12 September 2011)

The iron potassium fluorides with the general formula $K_x Fe^{II}_x Fe^{III}_{5-x} F_{15}$ $(2 \leqslant x \leqslant 3)$ are interesting multiferroic materials, for which the coexistence of all the three ferroic orders (elastic, electric, and magnetic) is simultaneously observed below the magnetic transition. Although the phase diagram has been previously defined, in particular for the potassium-rich $K_3Fe_5F_{15}$ phase, its complex magnetic behavior has not been completely understood. In this paper, the information obtained by magnetization measurements carried out on an oriented single crystal, revealing high anisotropy with coercive field reaching 14 kOe on the easy axis, are combined with Mössbauer spectroscopy and powder neutron diffraction data to define the magnetic structure. The ferrimagnetic behavior of $K_3Fe_5F_{15}$ arises from an antiferromagnetic triangular spin system, determined by neutron diffraction, frustrated by the difference in the magnetic contributions of adjacent structural layers, originated by Fe(II)/Fe(III) charge ordering. The atomic moments corresponding to the different iron sites, which cannot be reliably refined by neutron data, were evaluated from the hyperfine fields and quadrupolar parameters derived from Mössbauer measurements, by taking into account the saturation magnetization measured along the b easy axis. The complexity of the $M(H)$ and $M(T)$ measurements in the $H//a$ case is explained by the existence of an alternative magnetic solution, originated by the pseudotetragonal character of the structure, that is thermodynamically unfavorable in spontaneous magnetization, but becomes accessible when an external magnetic field is applied along a.

PACS number(s): 61.05.fm, 75.30.−m, 75.85.+t, 76.80.+y

I. INTRODUCTION

Multiferroics are materials presenting the coexistence of at least two ferroic orders among ferroelectricity, ferromagnetism, and ferroelasticity.[1] This class of compounds, albeit rare when magnetism is involved, is attracting wide interest: on one hand, the synthesis of magnetoelectric materials is a challenging task in the field of materials engineering since ferroelectricity and magnetism seem to be mutually exclusive phenomena;[2] on the other hand, the understanding of the possible conditions of coexistence of the ferroic orders and their complex interplay mechanisms are fundamental issues in solid state physics. Moreover, some perspectives in the applicative field are extremely appealing, involving the realization of devices controlled, for example, by both magnetic and electric fields, as well as the chance offered by materials able to exploit more than one task at a time, in particular within the picture of a constant rush towards miniaturization.[3] The iron potassium fluorides with the general formula $K_x Fe^{II}_x Fe^{III}_{5-x} F_{15}$ are interesting multiferroic materials where the coexistence of all the three ferroic orders is observed simultaneously.[4] By the structural point of view, these compounds belong to the class of tetragonal tungsten bronzes (TTBs), a term originally used to indicate the nonstoichiometric compound $K_x WO_3$ $(x = 0.4−0.6)$,[5] now extended to all the materials showing a similar structure. Noteworthy, several TTB niobates, as for example $Ba_2NaNb_5O_{15}$ (BNN), are ferroelectric and ferroelastic,[6,7] but since Nb^{5+} is in d^0 electronic configuration, no magnetic ordering can be observed. By substituting oxygen with fluorine, the TTB structure becomes accessible to low-valence transition metals carrying unpaired d electrons; as a consequence, magnetic ordering is allowed. Fluorides with TTB structure, firstly reported by De Pape[8] in 1965, show ferrimagnetic behavior[9–13] ascribed to the frustration of an antiferromagnetic spin structure. The existence of ferroelectricity in TTB fluorides has been reported for $K_3Fe_5F_{15}$,[14,15] being related to the shift of the iron ions off the center of the FeF_6 coordination octahedra, yielding nonzero dipole moment. The same feature is detected in $K_{2,62}Fe_5F_{15}$, where, in addition, the observation of cooperative tilting of the FeF_6 octahedra indicates the presence of ferroelasticity, in complete analogy with the phenomenon observed in BNN.[7,16] The axes of the ferroelastic superstructure are $a = 2a_{TTB}\sqrt{2}$, $b = a_{TTB}\sqrt{2}$, and $c = 2c_{TTB}$ so that diffraction intensities are observed with noninteger indices with respect to the fundamental TTB cell. Moreover, Fe^{II}/Fe^{III} ordering is detected in all the samples studied,[4,17,18] related to a charge ordering scheme which depends on the potassium content, as the general formula $K_x Fe^{II}_x Fe^{III}_{5-x} F_{15}$ $(2 \leqslant x \leqslant 3)$ suggests. For $x > 2.85$, an orthorhombic distortion of the fundamental tetragonal symmetry is reported to take place,[4,15] related to the formation of domains which may be associated to a further ferroelastic component involving the exchange of the a and b crystallographic axes. In 1994, Ishihara *et al.* suggested the presence of magnetoelectric coupling in $K_3Fe_5F_{15}$,[19] recently confirmed by the observation of a peak in the electric permittivity in correspondence of the magnetic ordering temperature.[20] Although the phase diagram of the compound with the highest potassium content has been defined quite accurately,[4] its complex magnetic behavior has

not been completely understood. In this paper, we combine the information obtained by magnetization measurements carried out on oriented crystals of $K_3Fe_5F_{15}$, Mössbauer spectroscopy and powder neutron diffraction data, to define the magnetic structure, a mandatory step in the understanding of the magnetoelectric behavior and coupling mechanisms occurring in this material.

II. EXPERIMENTAL

The synthesis of polycrystalline ceramic fluorides takes place by solid state reaction carried out in a nitrogen atmosphere in order to prevent the oxidation of the reactants. Hydrothermal technique was employed to produce large single crystals using $K_3Fe_5F_{15}$ powders as nutrient material and 40% hydrofluoric acid as a solvent. Detailed synthesis processes for both techniques are reported elsewhere.[4]

Neutron powder-diffraction data were collected with radiation wavelength $\lambda = 1.59$ Å at different temperatures, ranging from 5 to 300 K at the D2B beamline at the Laue-Langevin Institute in Grenoble.

The magnetic characterization was performed by means of a superconducting quantum interference device (SQuID) magnetometer (MPMS Xl Quantum Design, maximum applied field 5T) in the temperature range 5–300 K. In particular zero field cooling (ZFC) and field cooling (FC) curves were measured in an applied field of $H_a = 100$ Oe along different crystallographic axes. Moreover, $M(H)$ curves were measured at 5 K along different directions (i.e. a and b crystallographic axes) in an applied field range of $\Delta H = \pm 50$ kOe.

Mössbauer data were collected by means of a Wiessel spectrometer, calibrated by using a standard metal iron foil, and an Oxford flux cryogenic system with a base temperature of 1.8 K. Thirty-three spectra were collected between 2.2 K and room temperature in the absence of applied field: 15 of them are in a 5° range around the magnetic ordering transition temperature (T_N), five above 150 K, one at 2.2 K, and the others from 65 to 115 K.

III. RESULTS

The crystal structure of TTB fluorides is complicated by the simultaneous presence of charge ordering (involving, in our case, Fe^{2+}/Fe^{3+} cations) and cooperative tilt of the MF_6 octahedra (connected to ferroelasticity) modulations, each one with its own periodicity differently commensurate to the conventional TTB cell.[17] Charge order gives rise to a superstructure named COS (charge order superstructure), involving the doubling of the c parameter, which is twice in volume with respect to the fundamental TTB cell. On the contrary, the tilt modulation extends on a larger periodicity, giving rise to a supercell named FES (ferroelastic superstructure) that is eight times in volume the fundamental TTB cell. This modulation is strictly similar to that found at room temperature in ferroelectric BNN,[7] where it is related to the onset of ferroelasticity. A detailed crystal structure analysis of $K_3Fe_5F_{15}$ has been previously reported on the basis of single crystal x-ray diffraction (XRD) data.[4] The determined charge ordering scheme, where Fe^{2+} and Fe^{3+} ions tend to alternate
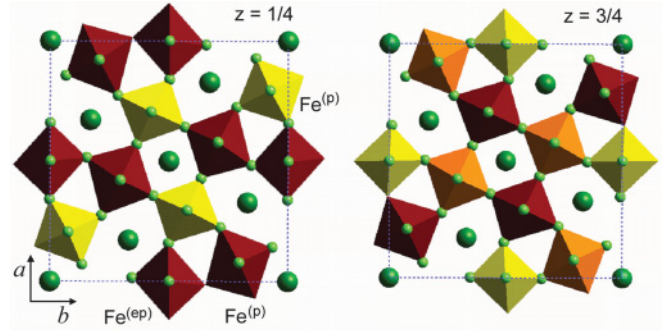

FIG. 1. (Color online) Projection of the COS structure onto the ab plane showing the different charge order characterizing the two layers stacked along the [001] direction at $z = \frac{1}{4}$ and $\frac{3}{4}$. Fe(II), Fe(III), and mixed-valence sites are evidenced in red (dark grey), yellow (light grey) and orange (intermediate), respectively; perovskite and extraperovskite-type sites are indicated as $Fe^{(p)}$ and $Fe^{(e-p)}$, respectively, following the notation used in the discussion of the Mössbauer results.

along the c axis in order to minimize the distortion, is reported in Fig. 1. Both perovskite and extraperovskite sites [indicated as $Fe^{(p)}$ and $Fe^{(e-p)}$, respectively] are engaged in the charge ordering, assuming different characteristic on adjacent layers: at $z \approx 0.25$, the $Fe^{(e-p)}$ site is occupied by Fe^{2+}, whereas Fe^{2+} and Fe^{3+} alternate around the perovskite cage in the $Fe^{(p)}$ sites; at $z \approx 0.75$, the $Fe^{(e-p)}$ site is occupied by Fe^{3+}, whereas around the perovskite cage mixed $Fe^{(p)}$ sites (occupied statistically by Fe^{2+} or Fe^{3+}) alternate with Fe^{2+} sites. This arrangement that represents the best compromise to minimize the structural stress in the structural stacking will be used as starting information in the present work.

A. Magnetic characterization

In a previous work,[4] we have shown that $K_3Fe_5F_{15}$ displays anisotropic ferrimagnetic behavior with the magnetization in the ab plane orders of magnitude larger than in the c direction. In this paper, we extend this study, exploring separately the independent crystallographic directions. Several crystals were checked by XRD in order to find an untwined individual of suitable dimensions. Finally a $1.5 \times 0.5 \times 0.2$ mm^3 needle, elongated along the c axis, was selected in order to perform a thorough magnetic characterization. The curves relative to zero field cooled (ZFC) and field cooled (FC) measurements, performed with applied field $H = 100$ Oe, except for the c direction, for which a field of $H = 500$ Oe was applied to improve the S/N ratio, reported in Fig. 2, were measured with the magnetic field applied in turn parallel to the a, b, and c axes. Inverse susceptibility reveals the antiferromagnetic nature of the exchange interactions, being the Curie–Weiss temperature $\Theta \approx -(1098 \pm 113)$ K along b, $\Theta \approx -(1305 \pm 276)$ K along a, while in the case of the hard axis, the calculated Θ is strongly reduced, $\Theta \approx -(422 \pm 61)$ K along c. In the inset of Fig. 2, an example of the FC curve measured along the b direction is reported in terms of χ_M^{-1}. However, the ZFC curves collected with applied field both in the a and b directions show the setting of nonzero magnetization below 116 K, evidencing a ferrimagnetic behavior of the system, likely originated by a strong frustration of an antiferromagnetic
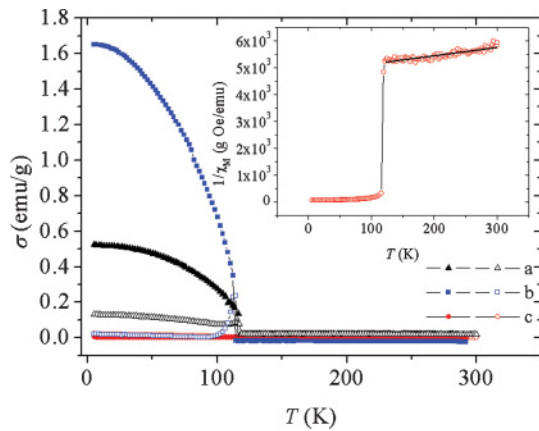
FIG. 2. (Color online) Zero field cooled (empty symbols) and field cooled (filled symbols) mass susceptibility (χ_M) curves measured applying the magnetic field $H = 100$ Oe along a (black triangles) and b (blue squares) crystallographic directions and $H = 500$ Oe along c (red dots). Inset: $1/\chi_M$ FC curve measured along the b direction.

structure, as confirmed by the value of $|\Theta|/T_N \approx 9.5$ along the a and b directions. Noteworthy, a typical Curie–Weiss behavior detected in the inverse susceptibility curve above 200 K is shown (inset of Fig. 2), becoming almost temperature independent below this temperature. This feature suggests the presence of Van Vleck paramagnetism, which may be related to a change in the electronic structure of the system. The sample shows large magnetic anisotropy: the in-plane (ab) magnetization is of the order of 1 emu/g, two orders of magnitude larger than along c. As expected by symmetry considerations, the a and b directions result to be nonequivalent, not only in terms of absolute magnetization at 5 K, but also in the magnetization loop shape. The largest low-temperature magnetization is observed along the b axis, being $M_b = 1.7 \pm 0.1$ emu/g at 5 K in the FC measurement for an applied field of 100 Oe. Moreover, the sharp peak detected near T_N in the corresponding ZFC curve confirms the presence of strong anisotropy. By increasing T, a net magnetization close to zero is retained up to a few Kelvin below the ordering temperature, where the field applied in the measurement (100 Oe) becomes large enough to reorient the domains. This unambiguously indicates the b axis as the easy magnetization direction. In spite of this, the magnetic behavior in FC along the a direction is quite similar, even if a significantly lower low-temperature magnetization is detected ($M_a = 0.5 \pm 0.1$ emu/g, reduced by a factor of three with respect from the easy axis value) at 5 K in the same experimental conditions. However, the ZFC behavior differs completely in this case, giving an appreciable (and almost T independent) response in the whole temperature range below T_N.

A remarkable difference between the a and b orientations is also offered by the $M(H)$ measurements performed at 5 K (Fig. 3). The hysteresis loop measured with the magnetic field applied along b shows a square shape typical of a hard magnet with a saturation magnetization $Ms_b = 2.6 \pm 0.1$ emu/g and a coercive field $H_C = 14$ kOe. On the contrary, the one measured with the magnetic field applied along a shows a constrained and asymmetric shape. The saturation magnetization is lower
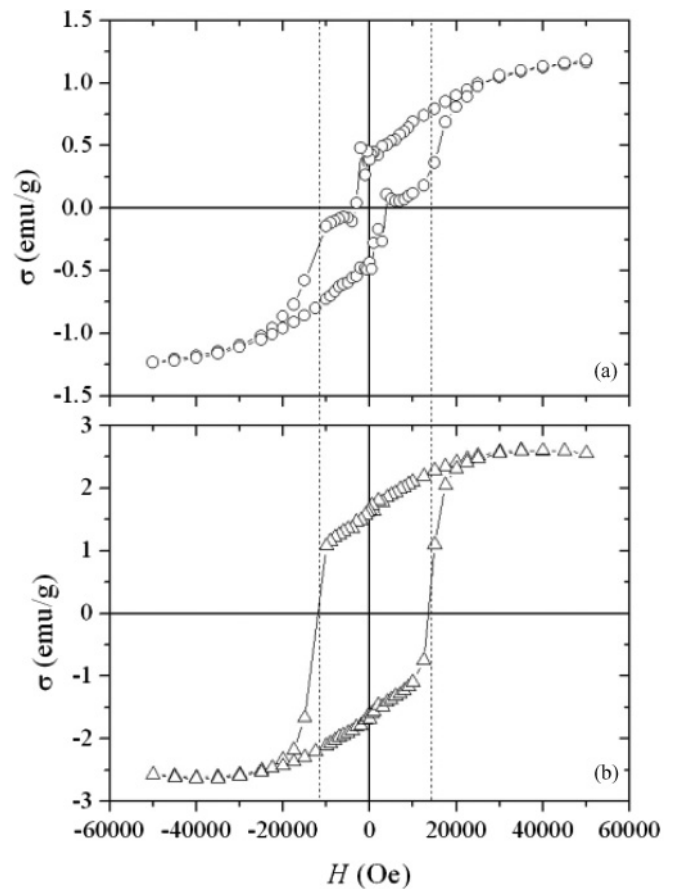

FIG. 3. Hysteresis loop at 5 K measured (a) along a direction and (b) along b axis. The vertical dashed lines are guides to the reader's eye and show the onset of instability of the magnetic moments aligned along a direction when the magnetic field is reduced and raised up from saturation.

($Ms_a = 1.2 \pm 0.1$), while the coercivity is of the order of 3 kOe. A satisfactory explanation of the magnetic behavior cannot be advanced without the knowledge of the magnetic structure; as a consequence, the discussion of the peculiar $M(H)$ loops shape is postponed to the conclusions section.

B. Neutron diffraction

Neutron powder-diffraction data were collected at different temperatures, ranging from 5 K to room temperature (RT), using 1.59 Å wavelength in the 2θ range 10–140° with step 0.05°. The appearance of magnetic peaks is observed, as expected, below 118 K. However, the data show a significant increase of the magnetic background in the 118–200 K region, in correspondence of the variation of the slope of the inverse susceptibility revealed by magnetization measurements. This could be produced by short-range magnetic interactions, giving rise to diffuse scattering in the low-angle region of the diffraction pattern. This hypothesis finds an indirect confirmation in a series of nuclear magnetic resonance (NMR) studies performed on the isostructural compound $K_{2.5}Mn_{2.5}Fe_{2.5}F_{15}$, suggesting the presence of spin glass below 200 K.[21] Rietveld refinements of neutron powder-diffraction data were carried out on the data collected at
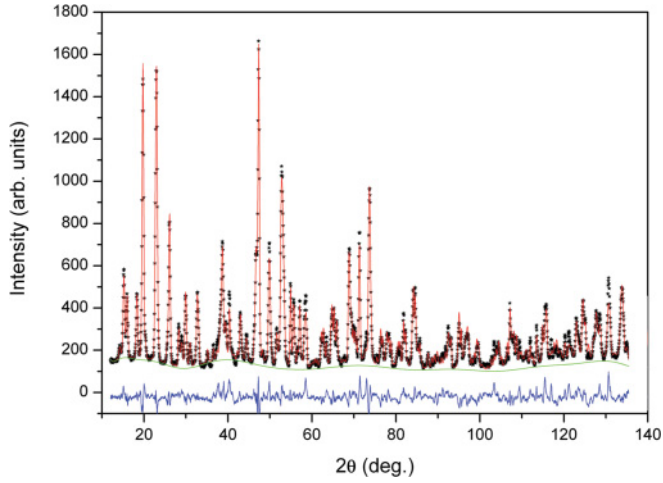
FIG. 4. (Color online) Rietveld plot of the neutron diffraction data taken at 5 K, showing the comparison of the observed (black dot) and calculated (red line) intensity. The difference is shown at the bottom as a blue line.

5 K using the GSAS package.[22,23] The patterns were indexed on the basis of a $Pb'a2'$ cell [$a = 12.697(1)$, $b = 12.598(1)$, $c = 7.919(1)$], the same being reported for the structurally related compound $K_3(FeMn)_5F_{15}$.[24] The composition of the studied sample was determined by the refinement of the potassium occupancy as $K_{2.93}Fe_5F_{15}$, evidencing a slight potassium deficiency with respect to the nominal composition. Owing to the limited magnetic information and to the high number of independent parameters, the achievement of final convergence in the refinement of the spin ordering scheme, initially obtained by refining all the components of the independent atomic moments as free variables, required the definition of a simplified model by imposition of constraints/restraints. At first, the z components obtained in the free model being very small, they were constrained to zero in agreement with the magnetic measurements performed on single crystal. Moreover, where similar values of the spin components along x and y were obtained, constraints were introduced, yielding a magnetic ordering scheme in which the atomic moments within the two layers, equal in modulus, are coupled antiferromagnetically. The refinement converged with agreement factors $wRp = 0.078$, and $R(F^2) = 0.086$ and $\chi^2 = 1.511$; the Rietveld plot is reported in Fig. 4, while the structural and magnetic data are resumed in Table I. In the refined model, the spins are forced to lie in the ab plane, so that the z resultant of the moment is zero, in agreement with the magnetization measurements. At the same time, the symmetry conditions impose also the x resultant to be zero, while nonzero values are allowed only in the y direction. However, the two independent layers stacked along the crystallographic c direction being coupled antiferromagnetically, the resultant moment is equal to zero, in evident contrast with the magnetization measurements. This clearly results from the oversimplified model, where all the atomic moments are constrained to be equal. In reality, a correct evaluation of the resultant moment must consider the simultaneous presence in the structure of ordered Fe^{2+} and Fe^{3+} ions carrying different atomic moments that modify the geometric antiferromagnetic arrangement.

TABLE I. Saturation mass magnetization σ_s (ZFC and FC curves) measured at 5 K along the three different crystallographic directions. Along c, the applied field is $H = 500$ Oe, while along a and b, a field of $H = 100$ Oe was used.

Direction	σ^{ZFC}(5K) (emu/g)	σ^{FC}(5K)(emu/g)
a (100 Oe)	0.133 ± 0.011	0.524 ± 0.044
b (100 Oe)	0.038 ± 0.004	1.65 ± 0.14
c (500 Oe)	0.022 ± 0.002	0.113 ± 0.008

C. Mössbauer spectroscopy

The sample was prepared by mixing the active material powder with Boron nitride as eccipient and contains $8.2 \, \text{mg cm}^{-2}$ of natural iron. A qualitative comparison between powder XRD spectra collected at ambient temperature on both the sample and the active material powder does not show target orientation. In order to check this, we compared Mössbauer spectra collected at room temperature for two different orientations of the target with respect to the optical (gamma ray) axis: the former with $\alpha = 0$ and the latter with $\alpha = 57°$ (magic angle). For both the spectra, we obtained the same cross-section values, and thus we can deduce a random orientation of the crystallites in the target (see Fig. 5).[25] All of the collected spectra show broadened lines, which display substructures, as expected in a spectrum arising from a set of similar contributions. Moreover, the high temperature spectra [Fig. 6(b)] clearly show the coexistence of nonequivalent contributions from both Fe(II) and Fe(III) ions. This feature leads also to the asymmetry displayed in the low-temperature spectra [Fig. 6(a)]. The fitting procedure was performed using the transmission integral method[26] and describing the resonant recoilless cross section throughout Voigt profiles.[27,28] In order to describe the different contributions to the spectra, the sites of the iron ionic species are denoted as follows:
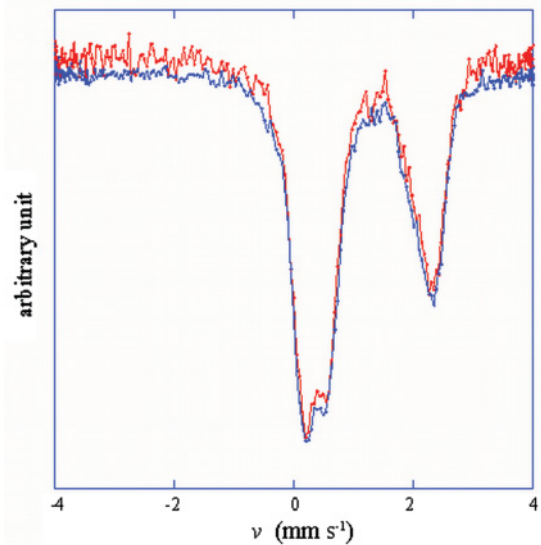

FIG. 5. (Color online) Comparison of Mössbauer spectra collected at room temperature for two different orientations ($\alpha = 0$ and $57°$) of the target with respect to the optical (gamma ray) axis, suggesting random orientation of the crystallites in the target.
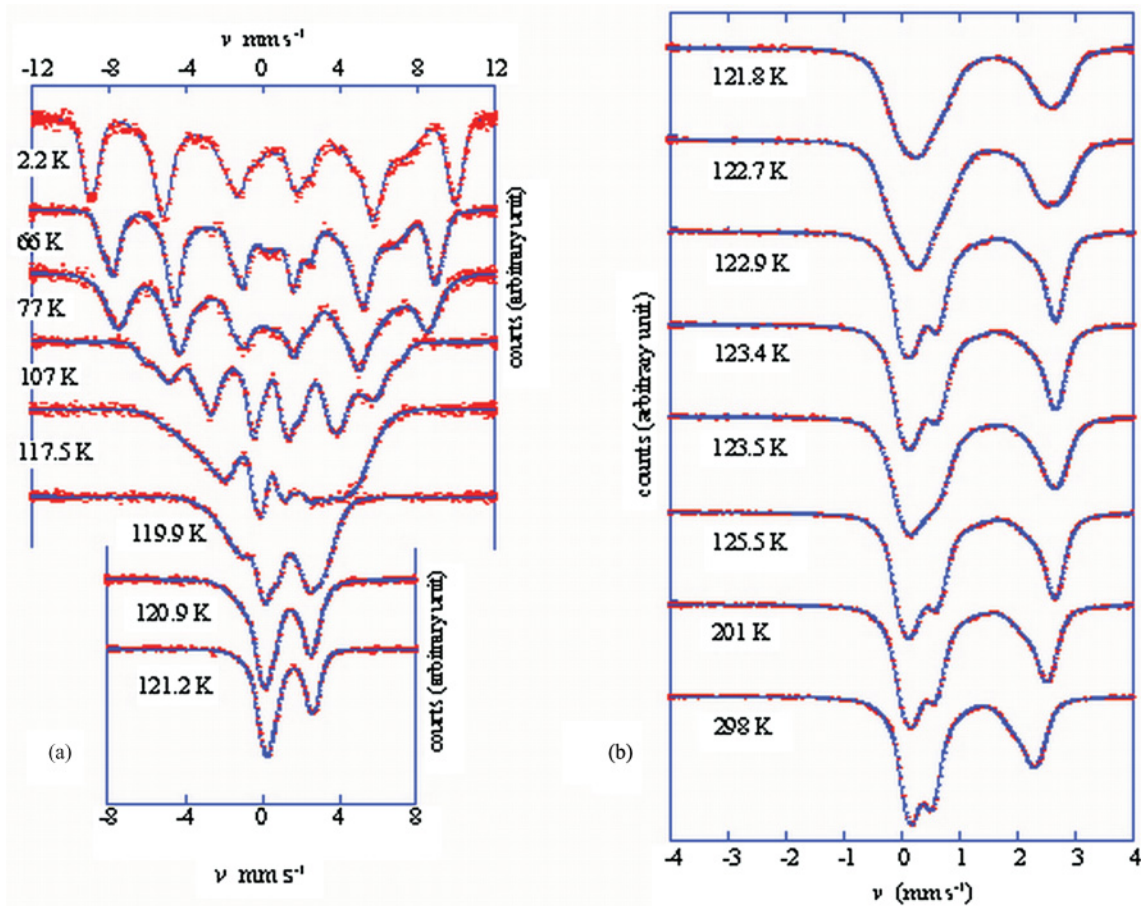
FIG. 6. (Color online) Selection of the recorded Mössbauer spectra: (a) low-temperature spectra ($T \leqslant T_N$), (b) high-temperature spectra ($T \geqslant T_N$).

(1) Fe(III) extraperovskite site (Fe2, multiplicity = 2) = $>\mathrm{Fe}_3^{(e-p)}$

(2) Fe(III) perovskite site (Fe5, multiplicity = 4) = $>\mathrm{Fe}_3^{(p)}$

(3) Fe(II) extraperovskite site (Fe1, multiplicity = 2) = $>\mathrm{Fe}_2^{(e-p)}$

(4) Fe(II) perovskite site (Fe3 and Fe6, multiplicity = $4 + 4 = 8$) = $>\mathrm{Fe}_2^{(p)}$.

From structure analysis, four mixed valence sites (Fe4) have to be added to the previous ones. In agreement with the assumption of a low-frequency jump of valence with respect to the iron Mössbauer line width (1.16 MHz), we chose to describe the corresponding contribution to the spectra by two component subspectra, instead of only one of double multiplicity, denoted as follows:

(5) Fe(III) perovskite site (Fe4, multiplicity = 2) = $>\mathrm{Fe}_{3m}^{(p)}$

(6) Fe(II) perovskite site (Fe4, multiplicity = 2) = $>\mathrm{Fe}_{2m}^{(p)}$.

Each site is characterized by an electric quadrupolar interaction and a magnetic hyperfine field, whose orientation with respect to the local electric field gradient (EFG) tensor changes from site to site. To take into account sample inhomogeneity, we introduce Gaussian distributions for the parameters. This procedure results in a cross section based on Voigt profiles whose Lorentian components are fixed to the natural values, and the Gaussian ones are related to the chosen parameters' distributions. The field orientation can be extracted, and in a

partial way, from the spectra only for the Fe(II) sites because, for them, the quadrupolar and the magnetic interactions have the same order of magnitude: the extractable quantity is an invariant function of the polar angles[29] so that we are allowed to force the azimuth angle to zero. On the contrary, for Fe(III) sites, the corresponding spectra are sensitive only to the EFG component along the magnetic field direction. Fe(II) and Fe(III) sites differ also for the value of the chemical shift (δ_{IS}) and for the Debye–Waller factor (f), which is related to the ion mean square displacement. For the sake of simplicity, we assumed that all the Fe(III) ions share the same value of f and analogously for the Fe(II) ions. Thus, the Mössbauer thickness is proportional to the multiplicity only within any ionic species.

Let us examine the trends with the temperature of the Fe(III) [$t_a^{(3)}$] and Fe(II) [$t_a^{(2)}$] thickness contributions, Fig. 7. First of all, we note the fall down of $t_a^{(2)}$ at T_N, while the Fe(III) contribution follows the expected continuous behavior corresponding to a Debye temperature of about 290 K, apart from a small range around T_N. Below the transition temperature, the ratio between the contributions to t_a due to the two ionic species is 2:3, as expected from stoichiometry. It rises up to about 0.85 at T_N, and then it slowly decreases down to 0.78 at room temperature (see Fig. 7).

The mean square displacements corresponding to $t_a^{(2)}$ and $t_a^{(3)}$ are illustrated in Fig. 8: for 65 K $< T < T_N$ the
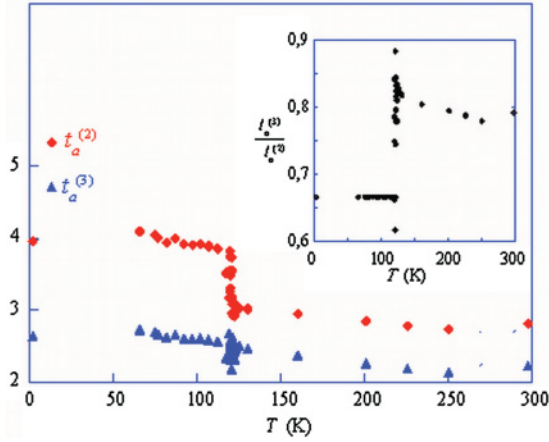
FIG. 7. (Color online) Dependence of the Mössbauer thickness for the Fe(III) and Fe(II) iron ions on the temperature: the trend of their ratio is shown in the box.

two ionic species have the same value, which goes from 2.5×10^{-3} to 4×10^{-3} Å^2; at T_N, both of them undergo a sharp increasing up to $\approx 6 \times 10^{-3}$ Å^2 for Fe(III) and to $\approx 9 \times 10^{-3}$ Å^2 for Fe(II), just above T_N $\langle x^2 \rangle^{(3)}$ comes back to the previous value while $\langle x^2 \rangle^{(2)}$ takes the value of 8×10^{-3} Å^2, then both of them follow the expected thermal trend. The values for the extreme temperatures don't follow the described trend: the ones at 2.2 K are larger than expected, while the ones at ambient temperature would indicate a hardening of the material. The strong increasing of the vibrational amplitude of Fe(II) ions at T_N appears to be connected with the loss of magnetic ordering, indicating a strong magnon-phonon coupling. In ferroelectrics, sharp peaks of $\langle x^2 \rangle$ are usually related to the FE transition.[30] Since our material is ferroelectric above and below T_N, the sudden enhancement of $\langle x^2 \rangle^{(2)}$ is not due to processes connected with the establishment of the FE phase but rather to a low-temperature anharmonic effect.
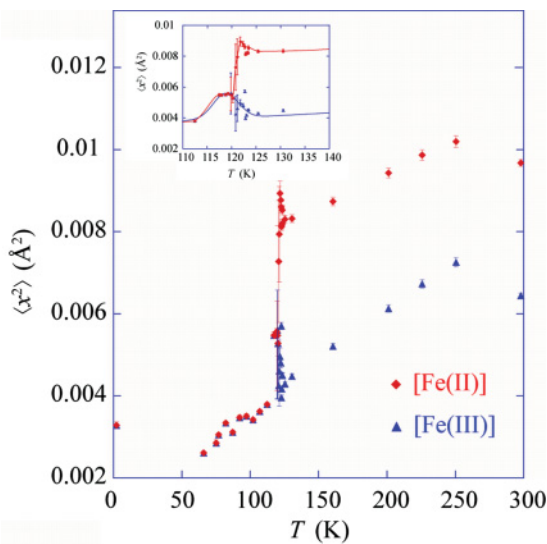

FIG. 8. (Color online) Temperature dependence of the mean square displacements, along the optical axis, of Fe(III) and Fe(II) ions: for $T < T_N$, the two trends coincide. In the inset, an enlarged display around T_N is also shown.
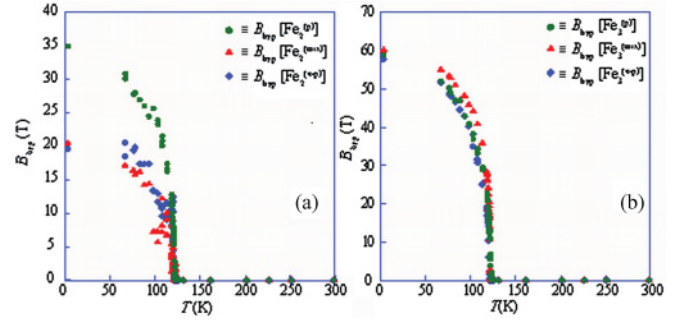

FIG. 9. (Color online) Temperature dependence of the hyperfine field at the three sites (a) of Fe(II) and (b) of Fe(III).

Such anharmonicities are present in many FE compounds,[31] and we suppose that in our case they are locked below T_N by the magnetic coupling of Fe(II) ions to Fe(III) ones. This assumption is also supported by the sharp increasing of $\langle x^2 \rangle^{(3)}$ just below T_N, since the residual magnetic interaction links Fe(II) and Fe(III) vibrational motions.

The hyperfine field trends with T for Fe(II) and Fe(III) ions are illustrated in Fig. 9. The Gaussian broadening for each site results to be ≈ 3 T in the whole range of temperatures. All the fields fall down at 122 K, a few degrees above the transition temperature estimated by the magnetization measurements: the small difference is due to the different time resolution of the two techniques. The saturation values B_0 of the hyperfine field obtained at 2.2 K are reported in Table II for the six sites.

The hyperfine field arises from three contributions: the Fermi-contact field, that depends on the unpaired d electrons, the orbital one, that is connected to the L_z mean value, and the dipolar field produced by the total spin magnetic moment of the valence electrons.[32] The values of B_0 for Fe(III) sites are typical of purely ionic high-spin sites ($S_z = 5/2$). Regarding the Fe(II) sites, Fe$_2^{(p)}$ is surely a high-spin one, while in order to determine the spin values of the others we need to analyze also the corresponding quadrupolar splittings. The hyperfine field orientation can be estimated for Fe$_2^{(p)}$ site with respect to the EFG principal axes obtaining $\theta = 1.2 \div 1.3$ rad.

As far as the hyperfine electric parameters are concerned, we start from considering the isomer shift behavior for the different iron sites. At the lowest temperature, the value is the same for any ionic species: $\delta_{IS} \approx 0.4$ mm/s for Fe(III) and ≈ 1.4 mm/s for Fe(II), in agreement with the typical values reported in literature for Fe(III) and high-spin Fe(II), respectively. At T_N, we have sharp variations of the parameter, and above T_N, the trends for every site become regular and almost independent of T. Just above the transition, we have $\delta_{IS} \approx 1.7$ mm/s for Fe$_{2m}^{(p)}$, ≈ 1.0 mm/s for Fe$_2^{(e-p)}$, ≈ 0.6 mm/s for Fe$_{3m}^{(p)}$, and ≈ 0.1 mm/s for Fe$_3^{(e-p)}$. Noteworthy is that the values for Fe$_3^{(p)}$ and Fe$_2^{(p)}$ sites do not change by trespassing the transition temperature: this behavior means that the magnetic transition does not cause a variation of d electrons total population. On the contrary, for the other sites, the observed variations suggest a decrease of d electrons total population for extraperovskite sites Fe$_3^{(e-p)}$ and Fe$_2^{(e-p)}$ and a mirrorlike increase for the mixed ones Fe$_{2m}^{(p)}$ and Fe$_{3m}^{(p)}$. About the quadrupolar splitting,

TABLE II. Refined parameters of nuclear and magnetic structure.

Atom	x	y	z	U_{iso}(Å²)	M_x (μ_B)	M_y (μ_B)	M_z (μ_B)	$\lvert M\rvert$ (μ_B)	Φ (°)	Θ (°)
K1[a]	$\frac{1}{2}$	$\frac{1}{2}$	$-0.016(20)$	0.011(3)						
K2[a]	0	0	0.467(18)	0.011(3)						
K3	0.677(18)	0.168(16)	0.007(13)	0.007(2)						
K4	0.166(19)	0.329(15)	0.503(12)	0.007(2)						
Fe1	$\frac{1}{2}$	0	0.253(11)	0.004(1)	4.20(1)	0	0	4.20(1)	90	0
Fe2	$\frac{1}{2}$	0	0.749(12)	0.004(1)	$-4.20(1)$	0	0	4.20(1)	90	180
Fe3	0.424(2)	0.286(2)	0.253(10)	0.004(1)	$-3.45(4)$	$-2.40(4)$	0	4.20(4)	90	$-145.2(5)$
Fe4	0.424(2)	0.286(2)	0.751(11)	0.004(1)	3.45(4)	2.40(4)	0	4.20(4)	90	34.8(5)
Fe5	0.212(2)	0.074(2)	0.253(10)	0.004(1)	$-3.45(4)$	2.40(4)	0	4.20(4)	90	145.2(5)
Fe6	0.214(2)	0.078(2)	0.749(10)	0.004(1)	3.45(4)	$-2.40(4)$	0	4.20(4)	90	$-34.8(5)$
F1	$\frac{1}{2}$	0	0.506(11)	0.029(1)						
F2	$\frac{1}{2}$	0	$-0.012(8)$	0.029(1)						
F3	0.415(6)	0.298(7)	$-0.009(9)$	0.029(1)						
F4	0.430(6)	0.289(7)	0.502(11)	0.029(1)						
F5	0.208(15)	0.065(11)	0.002(14)	0.029(1)						
F6	0.204(15)	0.088(11)	0.487(9)	0.029(1)						
F7	0.275(3)	0.217(3)	0.24(3)	0.029(1)						
F8	0.279(4)	0.224(3)	0.75(2)	0.029(1)						
F9	0.341(3)	$-0.002(3)$	0.256(2)	0.029(1)						
F10	0.349(3)	$-0.008(3)$	0.74(2)	0.029(1)						
F11	0.515(2)	0.155(3)	0.24(2)	0.029(1)						
F12	0.503(2)	0.154(3)	0.741(17)	0.029(1)						
F13	0.356(4)	0.433(5)	0.24(3)	0.029(1)						
F14	0.140(4)	$-0.066(5)$	0.74(3)	0.029(1)						
F15	0.571(3)	0.366(3)	0.25(3)	0.029(1)						
F16	0.067(3)	0.144(3)	0.75(3)	0.029(1)						

[a]Occupancy = 0.933

for Fe(III) sites, the values are included between 0.05 and 0.4 mm/s and are practically independent of T apart from a small range around the magnetic transition temperature. For Fe(II) sites, the behavior is more complex: at 2.2 K, all the values are at the top of the scale for this ionic species: 3.4 mm/s for $Fe_2^{(p)}$ and 2.7 mm/s for the others. This difference could be explained by a 0.1 electron fraction transfer from the excited doublet E_g to the ground triplet T_{2g}. This fact agrees with the observed change of asymmetry quadrupolar parameter η from 0 to 0.4. After T_N, $Fe_2^{(e-p)}$ and $Fe_2^{(p)}$ sites have the same values of Q_s at all the temperatures, while the $Fe_{2m}^{(p)}$ site shows much lower values (1.5 mm/s vs 2.5 mm/s, immediately after the transition). By increasing T, the quadrupolar splitting of all the sites decreases as it is expected for Fe(II) ions. The large drop of Q_s at T_N for the mixed site, with respect to the other ones, suggests a strong redistribution of d electrons population.

In order to evaluate the magnetic moments corresponding to the different iron sites, we need to merge the results coming from magnetization ($Ms_b = 2.62$ emu/g $= 0.806 \mu_B$ per unit cell), neutron powder diffraction (orientations of all the magnetic moments) and Mössbauer measurements (hyperfine fields and quadrupolar parameters for iron sites).

The B_0 values for Fe(III) sites of Table III suggest that for this ionic species the magnetic moments are respectively $\mu_3^{(e-p)} \approx 5$, $\mu_3^{(p)} = \mu_{3m}^{(p)} \approx 4.75$ in μ_B units, where the scaling, which has been assumed to be equal to one of the hyperfine fields, is due to small covalence effects. Regarding Fe(II) sites,

both quadrupolar splitting and isomer shift values suggest high-spin electronic states. On the other hand, for Fe(II) the orbital angular moment contribution B_L to the hyperfine field is not negligible. Since for a high-spin Fe(II), the Fermi-contact contribution, which is opposite to B_L, is about 50 T,[27] from B_0 values of Table III we can argue that B_L is larger for $Fe_2^{(e-p)}$ and $Fe_{2m}^{(p)}$ ions than for $Fe_2^{(p)}$ ones. Consequently, we expect the magnetic moment $\mu_2^{(p)}$ of the latter ion to be smaller than $\mu_2^{(e-p)}$ and $\mu_{2m}^{(p)}$. Moreover, taking always into account the Fe(II) high-spin state, by comparing the relative hyperfine fields, we can conclude that $\mu_2^{(e-p)} \approx \mu_{2m}^{(p)}$. The magnetic measurements suggest the a component of the magnetization per unit cell to be null. In this approximation, the magnetic moments of all the mixed sites with respect to the arrangement of the directions illustrated in Fig. 10 should be equal ($\mu_{2m}^{(p)} \approx \mu_{3m}^{(p)}$). Therefore, denoting by θ the angle between the magnetic

TABLE III. Saturation values B_0 of the hyperfine field obtained for the different Fe sites at 2.2 K and the corresponding estimated magnetic moments.

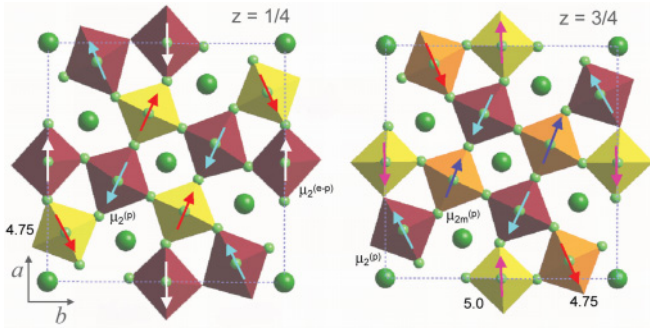|	$Fe_3^{(e-p)}$	$Fe_3^{(p)}$	$Fe_{3m}^{(p)}$	$Fe_2^{(e-p)}$	$Fe_2^{(p)}$	$Fe_{2m}^{(p)}$
B_0 (T)	60.1(2)	58.6(2)	57.5(3)	20.4(2)	34.7(2)	19.5(2)
m (μ_B)	5.0	4.75	4.75	4.75	4.6	4.75

FIG. 10. (Color online) Antiferromagnetic arrangement of the magnetic moments at the iron ions sites: orientations for all the moments are obtained by neutron powder diffraction; the values of the Fe(III) moments, derived from the corresponding saturation values of the hyperfine field B_0, are directly expressed in μ_B units; the Fe(II) moments are indicated by $\mu_2^{(e-p)}$, $\mu_2^{(p)}$, and $\mu_{2m}^{(p)}$ (see text for further details).

moments and a, the total magnetic moment per unit cell results:

$$m_{\text{tot}} = \left[0, 2\cos\theta\left(19 - 4\mu_2^{(p)}\right), 0\right].$$

By solving $m_{\text{tot}} = (0, 0.806, 0)$ with respect to $\mu_2^{(p)}$, we obtain $\mu_2^{(p)} = 4.75 - 0.10075 \sec\theta$. For θ values in agreement with neutron powder-diffraction measurements ($\theta \approx 35°$), $\mu_2^{(p)} \approx 4.6$.

We stress that both $\mu_{2m}^{(p)}$ and $\mu_2^{(p)}$ are greater enough than the value expected in the case of complete quenching of L ($\mu = 4$), but the orbital angular moment for the former is less quenched than for the latter. This result is in agreement with the corresponding values of B_0 reported in Table III, considering that the larger is the quenching of L, the larger is the total hyperfine field. Finally, we stress that the above assumption $\mu_{2m}^{(p)} \approx \mu_{3m}^{(p)}$ is not disappointing since the fraction of spin magnetic moment lost by Fe(II) ions with respect to Fe(III) ones is compensated by an incomplete quenching of the orbital angular moment.

IV. CONCLUSIONS

The magnetic properties of the orthorhombic phase $K_3Fe_5F_{15}$ determined on an oriented single crystal display a ferrimagnetic behavior originated by strong frustration of an antiferromagnetic structure. The magnetization measurements show large magnetic anisotropy with magnetization in the ab plane two orders of magnitude larger than in the c direction. As expected by symmetry considerations, the a and b directions result to be nonequivalent, not only in terms of absolute magnetization at 5 K, clearly indicating the b axis as the easy magnetization direction, but also in the characteristic features of the ZFC curve and in the shape of the magnetization loop. Whereas along a, the ZFC shows an appreciable (and almost T independent) response in the whole temperature range below T_N, along b, a sharp peak is detected near T_N; a net magnetization close to zero is retained on heating up to a few Kelvin below T_N, where the field applied in the measurement

(100 Oe) becomes large enough to reorient the domains (a typical signature of strong anisotropy).

The magnetic structure was solved and refined by powder neutron diffraction data on the basis a $Pb'a2'$ cell, metrically equivalent to the nuclear one utilized to describe the charge ordering. The atomic moments were found to lie in the ab plane oriented in three possible directions, determining a complex antiferromagnetic (AF) triangular spin system. Owing to the limited magnetic information contained in the diffraction patterns and to the high number of independent parameters required by the structural complexity, the final convergence was achieved by a simplified model in which the atomic moments are constrained to be equal in modulus. In this way, both the coupling on the single layer and between the layers being antiferromagnetic, the resultant moment is obviously null, in evident contrast with the magnetic measurements. In spite of this, the refined model is considered realistic; in fact the symmetry conditions impose the x resultant to be zero, so that a nonzero resultant (determined by differences in the atomic moments frustrating the AF order) is allowed only in the y direction, in agreement with the magnetization measurements indicating b as the easy axis. On the basis of this model, the magnetic moments corresponding to the different iron sites, which cannot be directly refined by neutron data, were evaluated from the hyperfine fields and quadrupolar parameters derived from Mössbauer measurements, by taking into account the saturation magnetization measured along the easy axis. The results are fully realistic and define in a complete way a magnetic structure that can be generally extended to the whole $K_xFe^{II}_xFe^{III}_{5-x}F_{15}$ system. In this scenario, the appearance of ferrimagnetic properties is mostly connected to the frustration of AF ordering produced by the charge ordering and in particular by the different charge distribution on the two adjacent AF-coupled structural layers. This is confirmed by the composition-dependent magnetization of these TTB fluorides, whose maximum is reached in the studied compound, for which the charge ordering (determined by structural analysis[4] and confirmed by the good fitting of the Mössbauer spectra obtained in this work) produces the maximal charge unbalance in the considered layers.

It is interesting to note that the magnetic structure successfully describes the magnetization measurements in the $H//b$ and $H//c$ cases, showing typical easy-axis and off-axis behavior, respectively, but apparently is not able to explain the complexity of the $H//a$ measurements. In fact, while symmetry conditions impose no resultant in this direction (as previously discussed), the FC magnetization, even if significantly lower, is of the same order of magnitude of the one detected along b. However, this can be understood by taking into account the pseudotetragonal character of the crystal structure. In fact for a tetragonal TTB structure, the magnetic structure would be described by two orthorhombic degenerate solutions, one with the resultant moment along b and a null component along a, described by the $Pb'a2'$ space group, and the other with the moment along a and a null component along b, described by the $Pba'2'$ space group. The structural distortion leading to the orthorhombic nuclear structure of $K_3Fe_5F_{15}$ removes the degeneration of the two magnetic solutions, making the former thermodynamically favored, but the latter accessible when an external magnetic field is applied along a.

This can explain also the differences revealed by the hysteresis loops reported in Fig. 3: in the $H//b$ case, the cycle has the typical shape determined by a hard behavior with a coercive field $H_{Cb} = 1.4$ T. On the contrary in the $H//a$ case the loop is constrained. The characteristic shape is determined by two factors. On one side, during the reversal of the magnetization, the domain moments are trapped in their natural orientation along b, determining the drastic drop of the magnetization along a as soon as the field is inverted. On the other one, by increasing the field, a critical value of the applied field (corresponding to the pinning field along b, slightly smaller than H_{Cb}) must be overcome to turn along a, in an efficient way, the magnetic moments.

[*] Corresponding author: francesco.mezzadri@nemo.unipr.it

[1] H. Schmid, Ferroelectrics **162**, 317 (1994).

[2] N. A. Hill, J. Phys. Chem. B **104**, 6694 (2000).

[3] M. Fiebig, J. Phys. D: Appl. Phys. **38**, R123 (2005).

[4] F. Mezzadri, S. Fabbrici, E. Montanari, L. Righi, G. Calestani, E. Gilioli, F. Bolzoni, and A. Migliori, Phys. Rev. B **78**, 064111 (2008).

[5] F. Wohler, Ann. Chim. Phys. **29**, 43 (1823).

[6] J. J. Rubin, L. G. Van Uitert, and H. J. Levinstein, J. Cryst. Growth **1**, 315 (1967).

[7] P. Labbè, H. Leligny, B. Raveau, J. Schneck, and J. C. Toledano, J. Phys. Condens. Matter **2**, 25 (1990).

[8] R. De Pape, C.R. Acad. Sci. **260**, 4527 (1965).

[9] E. Banks, M. Shone, R. F. Williamson, and W. O. J. Boo, J. Inorg. Chem. **22**, 3339 (1983).

[10] P. Lacorre, J. Pannetier, and G. Ferey, J. Magn. Magn. Mater. **94**, 331 (1991).

[11] S. Giri, K. Ghoshray, A. Ghoshray, and N. Chatterjee, J. Magn. Magn. Mater. **157**, 411 (1996).

[12] S. K. Mohammad Yusuf, L. Madhav Rao, R. Mukhopadhyay, S. Giri, K. Ghoshray, and A. Ghoshray, Solid State Commun. **101**, 145 (1997).

[13] S. C. Bhargava, S. Singh, A. H. Morrish, and Z. W. Li, Solid State Commun. **116**, 575 (2000).

[14] J. Ravez, S. C. Abrahams, and R. de Pape, J. Appl. Phys. **65**, 3987 (1989).

[15] J. Ravez, S. C. Abrahams, A. M. Mercier, L. Rabardel, and R. de Pape, J. Appl. Phys. **67**, 2681 (1990).

[16] P. B. Jamieson, S. C. Abrahms, and J. L. Bernstein, J. Chem. Phys. **48**, 5048 (1968).

[17] S. Fabbrici, E. Montanari, L. Righi, G. Calestani, and A. Migliori, Chem. Mater. **16**, 3007 (2004).

[18] Y. Calage, S. C. Abrahams, J. Ravez, and R. de Pape, J. Appl. Phys. **67**, 430 (1990).

[19] S. Ishihara, J. P. Rivera, E. Kita, Z. G. Ye, F. Kubel, and H. Schmid, Ferroelectrics **162**, 51 (1994).

[20] R. Blinc, G. Tavcar, B. Žemva, D. Hanžel, P. Cevc, C. Filipič, A. Levstik, Z. Jagličić, Z. Trontelj, N. Dadal, V. Ramachandran, S. Nellutla, and J. F. Scott, J. Appl. Phys. **103**, 074114 (2008).

[21] S. Giri, K. Ghoshray, A. Ghoshray, and N. Chatterjee, Phys. Rev. B **56**, 3347 (1997).

[22] A. C. Larson and R. B. Von Dreele, *General Structure Analysis System (GSAS)* (Los Alamos National Laboratory Report LAUR 2000) pp. 86-748.

[23] H. B. Toby, J. Appl. Cryst. **34**, 210 (2001).

[24] P. Lacorre, J. Pannetier, and G. Ferey, J. Magn. Magn. Mater. **94**, 331 (1991).

[25] J. M. Greneche and F. Varret, J. Phys. C: Solid State Phys. **15**, 5333 (1982).

[26] G. Spina, E. Pugliese, L. Cianchi, F. Del Giallo, M. Lantieri, and P. Moretti, J. Phys. Conf. Series **217**, 012015 (2010).

[27] J. Puerta and P. Martin, Appl. Opt. **20**, 3923 (1981).

[28] D. G. Rancourt, Nucl. Instr. and Meth. B **44**, 199 (1989).

[29] D. Satuła, K. Szymannński, L. Dobrzynński, V. H. Tran, and R. Trocć, Phys. Rev. B **78**, 014411 (2008).

[30] W. N. Rowan-Weetaluktuk, D. H. Ryan, A. O. Sushkov, S. Eckel, S. K. Lamoreaux, O. P. Sushkov, J. M. Cadogan, M. Yethiraj, and A. J. Studer, Hyperfine Interact. **198**, 1 (2010).

[31] R. E. Cohen, Nature **358**, 136 (1992).

[32] C. Yi-Long and Y. De-Ping, *Mössbauer Effect in Lattice Dynamics* (Wiley-VCH Verlag GmbH & Co. KGaA, Weinheim, 2007), p. 54.